DOI: 10.61782/fa.2025.0505

FORUM ACUSTICUM
EURONOISE 2025

INVESTIGATION OF THE INFLUENCE OF SLIP-OPERATORS ON ULTRASOUND PULSE-BASED SOUND GENERATION PRINCIPLES

Dominik Mayrhofer[1*] **Tobias Wilczacki**[1] **Manfred Kaltenbacher**[1]
[1] Institute of Fundamentals and Theory in Electrical Engineering,
Graz University of Technology, Austria

ABSTRACT

Ultrasound pulse-based sound generation principles like Advanced Digital Sound Reconstruction (ADSR) require fast-moving actuators operating in the micro-scale. In this contribution, we investigate the influence of solution-dependent slip-operators on the sound generation process of a unit cell for ADSR. The unit cell consists of a sound generation unit (loudspeaker) encased by two shutter gates, responsible for redirecting sound. For the numerical investigation, we solve the linearized compressible flow equations on moving domains coupled to structural mechanics and acoustics within a finite element context. Depending on geometric parameters, the sensitivity with respect to such effects as well as the performance can vary significantly. Here, we consider an extension of the linearized compressible flow equations up to a Knudsen number of 0.1. Besides the non-linear effect caused by slip-boundary conditions, the influence of finite mounting stiffness is investigated. Using a parameter study, we characterize the impact on the achievable sound pressure as well as the introduced asymmetry of the sound generation process.

Keywords: *Maxwell slip, ultrasound pulse-based sound generation, ADSR, linearized compressible flow, moving domains*

1. INTRODUCTION

In the past years, a clear trend towards the development of Micro-Electro-Mechanical-Systems (MEMS) loudspeakers could be observed [1–4]. Recent studies have shown that ultrasound pulse-based (USPB) sound generation principles used in MEMS loudspeakers can generate high sound pressure levels, especially in the low frequency range [5, 6]. The small form-factor combined with the higher achievable sound pressure level makes such MEMS loudspeakers ideally suited for in-ear applications. The underlying principle of USPB sound generation relies on a modulation of an ultrasound carrier signal. The modulation is achieved with a shutter device that changes the impedance of the outflow channel during the operation [5, 6]. For a sub-variant of sound generation principles called Advanced Digital Sound Reconstruction (ADSR) [5], the impedance change is done so that the shutter does not act as an additional source. The sound generation itself is achieved by modulating the carrier signal with the audio signal, which then gets modulated again by the changing impedance of the outflow channels. Overall, this creates a sound pulse that can be used to reconstruct an audio signal. Similar to the fundamental idea of Digital Sound Reconstruction [7, 8], multiple cells can be combined to enable a steady flow of air and therefore a continuous audio signal. In this contribution, a special version using a resonant excitation denoted as resonant ADSR is investigated [5].

The shutter itself is a crucial part of the underlying idea. In real applications, finite mounting stiffness can lead to undesired shutter movement, reducing the effectiveness of the system and introducing asymmetry. Due to the underlying operation principle containing moving shutters, it is crucial to incorporate domain movement to simulate the actual shutter movement and the corresponding impedance change. Therefore, the linearized compressible flow equations in Arbitrary Lagrangian-Eulerian (ALE) formulation are used to study viscous acoustics on small scales [9, 10]. Furthermore, leakage through the

*__Corresponding author__: dominik.mayrhofer@tugraz.at.

shutter plays a significant role with respect to the device's overall efficiency. Due to the small form-factor, viscous effects play an important role when simulating such devices [5, 11]. Depending on the actual size of the actuator, the so-called slip-flow regime is entered, where continuum theory starts to break down and particle interaction needs to be incorporated [12–14]. Extensions based on slip operators similar to the one described in [5] can be used to circumvent the limitation and extend the validity of the well-known simulation strategies. This workflow is already well established in computational fluid dynamics [13, 15, 16], but lacks application in acoustics. In this contribution finite element simulations are used to characterize the influence of slip boundary conditions and finite mounting stiffness on the achievable sound pressure output and the introduced asymmetry. For the simulation, the open-source multiphysics simulation tool *openCFS* is utilized [17].

2. GOVERNING EQUATIONS

In the next section, the underlying simulation framework is discussed.

2.1 Viscous acoustics

For the simulation of acoustic MEMS devices, the linearized compressible flow (LinFlow) equations can be utilized [10, 11]. In order to incorporate domain movement as well as slip boundary conditions (BCs), the extended LinFlow equations in Arbitrary Lagrangian-Eulerian (ALE) formulation are used [5]. The conservation of mass is given by,

$$\frac{1}{\rho_0\, c_0^2}\frac{\partial p}{\partial t} + \nabla\cdot\boldsymbol{v} - \frac{1}{\rho_0\, c_0^2}\boldsymbol{v}_\mathrm{g}\cdot\nabla p = 0, \tag{1}$$

whereas the conservation of momentum is given by

$$\rho_0\frac{\partial \boldsymbol{v}}{\partial t} - \rho_0\,(\boldsymbol{v}_\mathrm{g}\cdot\nabla)\boldsymbol{v} - \nabla\cdot[\boldsymbol{\sigma}_\mathrm{f}] + \boldsymbol{\lambda} = \boldsymbol{0}. \tag{2}$$

Furthermore, the fluid stress tensor $[\boldsymbol{\sigma}_\mathrm{f}]$ is given by

$$[\boldsymbol{\sigma}_\mathrm{f}] = -p\,[\boldsymbol{I}] + \mu_\mathrm{f}\,(\nabla\boldsymbol{v} + (\nabla\boldsymbol{v})^\intercal) + \left(\lambda_\mathrm{f} - \frac{2}{3}\mu_\mathrm{f}\right)(\nabla\cdot\boldsymbol{v})\,[\boldsymbol{I}]. \tag{3}$$

Here, ρ_0 denotes the mean density, c_0 the isentropic speed of sound, p the pressure, t the time and $\boldsymbol{v}$ the velocity. Furthermore, $\boldsymbol{v}_\mathrm{g}$ stands for the grid velocity, $[\boldsymbol{I}]$ for the identity tensor, μ_f the dynamic viscosity and λ_f is used for the bulk viscosity. Additionally, the Lagrange multiplier $\boldsymbol{\lambda}$ was introduced in (2) to incorporate slip boundary conditions given by

$$\boldsymbol{v} + \mathcal{S}^\mathrm{ic}(\boldsymbol{v}) - \boldsymbol{v}_\mathrm{g} = \boldsymbol{0} \quad \text{on } \Gamma_\mathrm{mSlip}(t). \tag{4}$$

This additional constraint equation incorporates the incompressible slip operator $\mathcal{S}^\mathrm{ic}(\boldsymbol{v})$ which is applied on the corresponding boundary $\Gamma_\mathrm{mSlip}(t)$. The slip operator itself returns a slip velocity $\boldsymbol{v}_\mathrm{slip}^\mathrm{ic}$ based on the fluid velocity

$$\boldsymbol{v}_\mathrm{slip}^\mathrm{ic} = \mathcal{S}^\mathrm{ic}(\boldsymbol{v}). \tag{5}$$

In the domain $\Omega_\mathrm{f}(t)$ itself as well as all boundaries not using slip boundary conditions,

$$\boldsymbol{\lambda} = \boldsymbol{0} \quad \text{on } \Omega_\mathrm{f}(t)\setminus\Gamma_\mathrm{mSlip}(t) \tag{6}$$

holds. At this point it is important to note that it is also possible to incorporate Lagrange multiplier directly in the weak form, where the boundary term arising from integration by parts as well as the additional contribution from the current Lagrange multiplier in (2) are combined to one Lagrange multiplier. Since investigations have shown that this formulation tends to be more stable [5], the second formulation is used in the simulations. For the sake of brevity, we refer to [5] for the derivation as well as the final formulation.

For the slip operator in (4), an incompressible slip operator is used, which is given by

$$\boldsymbol{v}_\mathrm{slip}^\mathrm{ic} = \frac{2-\sigma_\mathrm{v}}{\sigma_\mathrm{v}}\frac{\lambda_\mathrm{air}}{\mu_\mathrm{f}} ([\boldsymbol{I}] - \boldsymbol{n}_\mathrm{f}\otimes\boldsymbol{n}_\mathrm{f})\cdot(-\mu_\mathrm{f}\,(\nabla\boldsymbol{v} + (\nabla\boldsymbol{v})^\intercal)\cdot\boldsymbol{n}_\mathrm{f}). \tag{7}$$

The idea of the slip operator stems from computational fluid dynamics – see e.g. [13] – and has been applied to viscous acoustics [5].

2.2 Geometry deformation

For the mesh deformation various governing equations can be used [18]. In this case, a quasi-static solution of an artificial mechanics problem is applied [19], where the PDE will be denoted as the smooth PDE. The solution of the artificial mechanics problem provides the new coordinates used for the computation of the integrals. In contrast, the temporal change gives the grid velocity appearing in the conservation of mass and momentum given in (1) and (2), respectively. For the grid velocity, a backward

difference scheme of second order (BDF2 scheme) [19] is utilized. The smooth PDE itself is given by

$$-\nabla \cdot \left([\boldsymbol{C}_\mathrm{s}] : \frac{1}{2}(\nabla \boldsymbol{u}_\mathrm{s} + (\nabla \boldsymbol{u}_\mathrm{s})^\intercal) \right) = 0, \tag{8}$$

where $[\boldsymbol{C}_\mathrm{s}]$ is the artificial stiffness tensor and $\boldsymbol{u}_\mathrm{s}$ the artificial displacement. Since the smooth PDE introduces additional degrees of freedom (DOFs) which increase the computation time, the smooth PDE is only solved in regions where grid deformation is necessary. Considering the model setup depicted in Fig. 2, only the region "LinFlow ALE" is affected.

2.3 Acoustics

In order to reduce the computational time, the LinFlow equations are restricted to the region where they are necessary. Afterwards, we couple to the acoustic wave equation as soon as possible. This hybrid approach is also described in [5, 11]. An additional advantage of coupling to the acoustic PDE is that boundary conditions and features of the PDE like perfectly matches layers (PML) can be accessed. For the acoustic computations, the acoustic wave equation in pressure formulation is given by

$$\frac{1}{c_0^2}\frac{\partial^2 p_\mathrm{a}}{\partial t^2} - \nabla \cdot \nabla p_\mathrm{a} = 0, \tag{9}$$

where p_a represents the acoustic pressure. A direct coupling approach is used for the coupling between the LinFlow PDE and the acoustic PDE. Here, the continuity of surface traction given by

$$-p_\mathrm{a}\boldsymbol{n}_\mathrm{f} = [\boldsymbol{\sigma}] \cdot \boldsymbol{n}_\mathrm{f} \quad \text{on } \Gamma_\mathrm{NC} \tag{10}$$

as well as the continuity of normal acceleration

$$\frac{\partial \boldsymbol{v}}{\partial t} \cdot \boldsymbol{n}_\mathrm{f} = -\frac{1}{\rho_0}\nabla p_\mathrm{a} \cdot \boldsymbol{n}_\mathrm{f} \quad \text{on } \Gamma_\mathrm{NC} \tag{11}$$

are used. The coupling only occurs at the coupling interface Γ_NC, where non-conforming interfaces are utilized [20].

2.4 Mechanics

For the movement of the shutters, the mechanics PDE is used, which is given by

$$\rho_\mathrm{m}\frac{\partial^2 \boldsymbol{u}_\mathrm{m}}{\partial t^2} - \nabla \cdot \underbrace{\left([\boldsymbol{C}_\mathrm{m}] : \frac{1}{2}(\nabla \boldsymbol{u}_\mathrm{m} + (\nabla \boldsymbol{u}_\mathrm{m})^\intercal) \right)}_{[\boldsymbol{\sigma}_\mathrm{m}]} = \boldsymbol{f}_\mathrm{m}. \tag{12}$$

In (12) ρ_m denotes the density of the body, $\boldsymbol{u}_\mathrm{m}$ the mechanical displacement, $[\boldsymbol{C}_\mathrm{m}]$ the mechanical stiffness tensor, $[\boldsymbol{\sigma}_\mathrm{m}]$ the mechanical stress tensor and $\boldsymbol{f}_\mathrm{m}$ the forcing vector. For the suspension of the shutter, two individual points per shutter are used, which are incorporated as discrete points in the final system of equations. Additionally, coupling conditions to the smooth PDE as well as the LinFlow PDE are incorporated. For the smooth PDE, the displacement of the mechanics PDE is directly set for the smooth PDE as a Dirichlet boundary condition. The back-coupling caused by the surface traction at the fluid-structure interface is incorporated by taking the surface traction into account at the coupling interface Γ_mech via

$$[\boldsymbol{\sigma}_\mathrm{m}] \cdot \boldsymbol{n}_\mathrm{m} = [\boldsymbol{\sigma}] \cdot \boldsymbol{n}_\mathrm{m} \quad \text{on } \Gamma_\mathrm{mech}. \tag{13}$$

Here, $\boldsymbol{n}_\mathrm{m}$ is the normal vector pointing out of the mechanical domain.

2.5 Overall coupling framework

Based on the governing equations, the overall coupling framework can be defined. The visualization of the coupled framework implemented in *openCFS* [17] can also be seen in Fig. 1. It has to be noted that in Fig. 1 an additional path incorporating a contact force is depicted. The feature can be activated in principle, but it was not necessary for the computations presented in this contribution. Hence, the back-coupling patch is grayed out and not described in further detail for the sake of brevity.

3. SIMULATION SETUP

For the simulation setup, a similar 2D actuator as described in [21] is used. The device itself can be seen in Fig. 2 and has dimensions in the low micrometre range. Hence, the extended version of the LinFlow equations is used and compared to the standard one using only no-slip boundary conditions. The device consists of two channels that are connected with to a distribution chamber, where the excitation area representing a loudspeaker generates the air flow. In between, horizontally moving shutter gates are located which can open and close the path for air to flow in the respective channel. The excitation area is used to prescribe the inflow velocity and is denoted with Γ_exc. The inflow velocity in normal direction v_exc is given by

$$v_\mathrm{exc} = \hat{s}_\mathrm{mem}\, 2\pi\, f_\mathrm{shut}\, \sin(2\pi\, f_\mathrm{shut}\, t)\left(1 - e^{-t/\tau_\mathrm{shut}}\right), \tag{14}$$

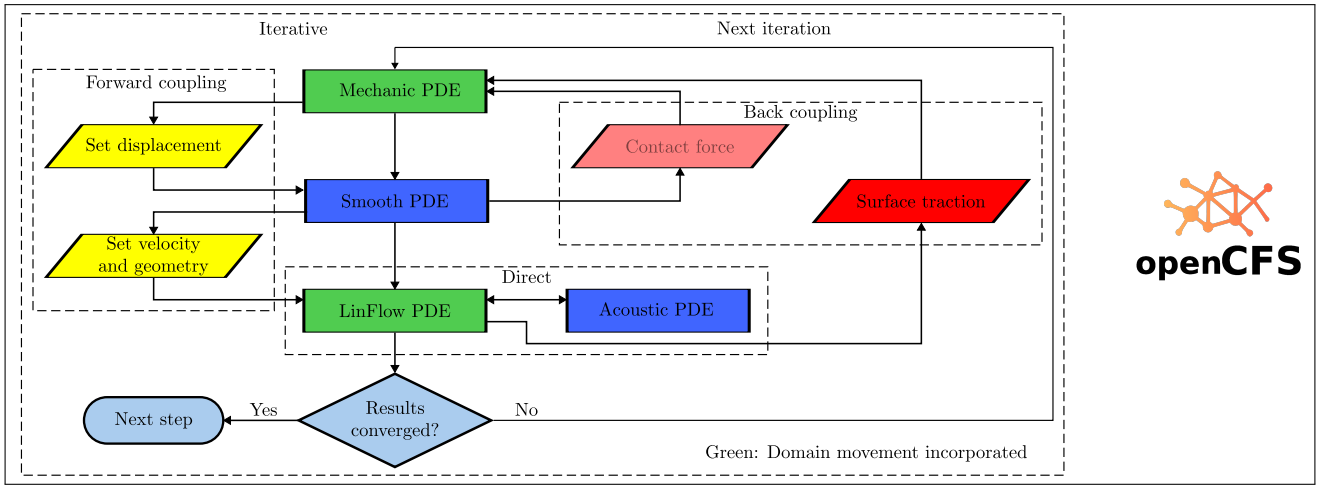

Figure 1. Visualization of the mixed iterative/direct coupling framework.

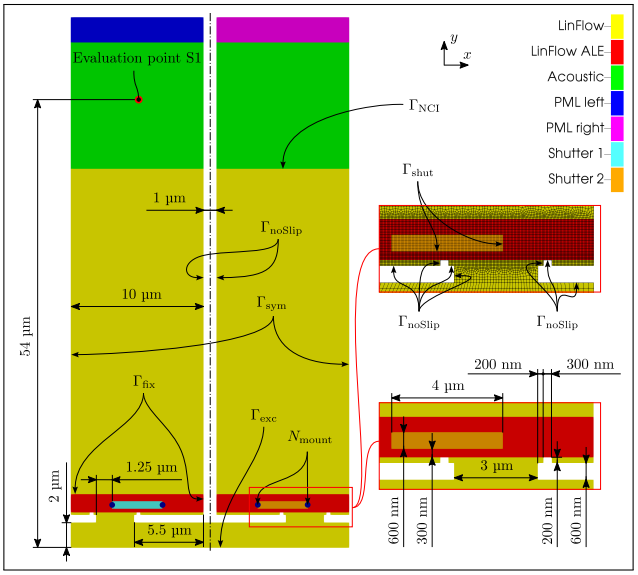

Figure 2. 2D model of a simplified actuator for resonant ADSR.

where $\hat{s}_{\text{mem}}$ is the displacement amplitude, f_{shut} the excitation frequency and τ_{shut} the time constant used for the fade-in. The parameters for these values are also given in Tab. 1. The two shutters directly above the distribution chamber are modeled in the center position to minimize the maximum displacement and therefore grid deformation, leading to better grid quality during the movement. Additionally, we prescribe the same displacement

Table 1. Excitation parameters for resonant ADSR.

Variable	f_{shut}	τ_{shut}	$\hat{s}_{\text{mem}}$	$s_{\text{shut,hor}}$
Value	48 kHz	$1/f_{\text{shut}}$	2.5 µm	1.75 µm

in x-direction for both shutters. Hence, when one shutter opens, the other closes, enabling the separation of sound pulses. The horizontal shutter displacement $s_{\text{shut,hor}}$ is given by

$$s_{\text{shut,hor}} = \hat{s}_{\text{shut}} \sin(2\pi\, f_{\text{shut}}\, t) \left(1 - e^{-t/\tau_{\text{shut}}}\right), \quad (15)$$

where $\hat{s}_{\text{shut}}$ is the shutter displacement amplitude given in Tab. 1.

The movement in the y-direction is not restricted and is governed by the mechanics PDE. For a more realistic mounting scenario, the mounting points N_{mount} are used to describe discrete values for the mounting stiffness. Here, realistic values from the parameter study in [22] are used. For the stiffness a value of $100\,\text{kN}\,\text{m}^{-1}$ and for the damping a value of $2\,\text{mN}\,\text{s}\,\text{m}^{-1}$ has been used. The movement in y-direction is caused by the surface traction stemming from the LinFlow PDE that can couple to the mechanics PDE at the coupling interface Γ_{shut}.

For the smooth PDE, which is only solved in the region denoted as "LinFlow ALE", the outer boundary is fixed at Γ_{fix}. At the interface Γ_{shut} the deformation from the mechanics domain is prescribed as Dirichlet values.

Regarding the LinFlow PDE, no-slip boundary conditions are used at Γ_{noSlip}, whereas symmetry boundary conditions are used at Γ_{sym}. To study the effect of Maxwell slip boundary conditions, the no-slip boundary conditions are replaced with slip boundary conditions at the former no-slip interfaces in the vicinity of the shutter. The affected surfaces also comprise Γ_{shut}, where the constraint equation also includes a non-zero grid velocity contribution. Additionally, the interface Γ_{NCI} is used to couple from LinFlow to acoustics with the help of a non-conforming interface. Above the acoustic domain, perfectly matched layers for each channel are used to ensure free radiation. In our setup the left channel is the main channel where we are interested in the acoustic response. Hence, an evaluation point denoted as "S1" is used to evaluate the acoustic pressure in this channel. In this case, the right channel is the side channel, where the pressure peaks will either be redirected such that they do not influence the sound generation process, or, ideally, damped out.

Finally, it has to be noted that the investigated simulation does not reflect the full operation mode of resonant ADSR but rather the generation of a pulse train. In order to generate an actual audio signal, the excitation velocity of the speaker needs to be modulated with the audio signal. Additionally, multiple of the investigated cells should be driven with a phase-shift of 90° to minimize ultrasound emission [5].

4. RESULTS

At first, field results in the vicinity of the shutter leading to the main channel are shown. Here, the simulation including no-slip boundary conditions with a suspended membrane is considered. Figure 3 shows the pressure and velocity distribution for the open position, where the maximum outflow occurs, whereas Fig. 4 shows the results for the closed position. Both figures also include a horizontal green line that shows the initial y-coordinate of the lower edge of the shutter. When the shutter is open, the outflow of the air can be observed. Additionally, the vertical movement of the shutter is close to zero, since the air can escape more or less freely. This can also be seen from the almost non-existent pressure gradient around the shutter. When the shutter is closed, the net flow through the main channel is not zero due to the imperfect sealing properties. Besides the leakage, a vertical displacement can be observed. Since the pressure inside the chamber is negative, the pressure gradient pulls the shutter downwards. For a positive pressure build-up inside the chamber, the

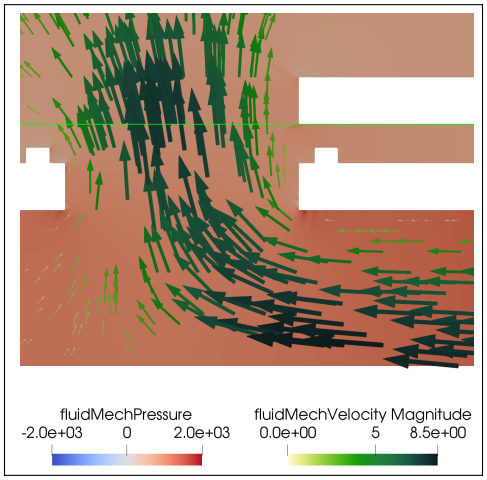

Figure 3. Pressure and velocity field near the left shutter in the open position.

effect would be inverted and the shutter would be pushed away from the distribution chamber. It has to be noted that this effect will inherently lead to asymmetry in the system, since the shutter displacement in y-direction also influences the residual height of the gap responsible for the leakage path. For negative pressure values, the shutter will be pulled closer, constricting the channel and leading to less leakage. For positive pressure values, the shutter will be pushed away, increasing the gap and therefore the leakage.

Besides the field results, four different combinations of effects are evaluated at S1. The four combinations are as follows:

- No-slip boundary conditions; shutter fixed in y-coordinate.
- Maxwell slip boundary condition; shutter fixed in y-coordinate.
- No-slip boundary conditions; suspended shutter (y-coordinate is not fixed).
- Maxwell slip boundary condition; suspended shutter (y-coordinate is not fixed).

The results at S1 for the four different setups are shown in Fig. 5, where close-ups in the regions of interest are used to highlight the differences. The results clearly show the influence on the achievable peak sound pressure is evident but overall relatively small. As expected, the combination of Maxwell slip boundary conditions and a suspended

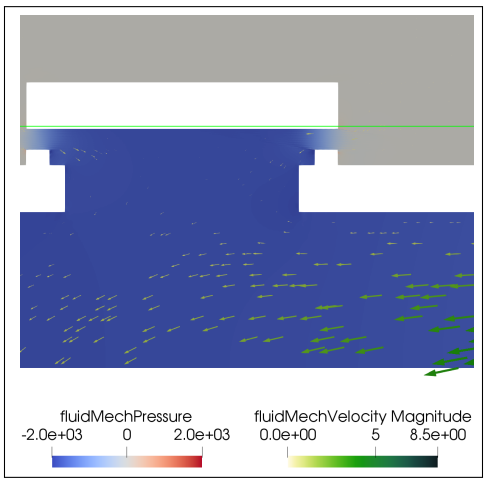

Figure 4. Pressure and velocity field near the left shutter in the closed position.

membrane leads to the highest leakage and therefore the lowest overall peak. It is important to note that the leakage responsible for the reduction of the overall peak is not the same as shown in the close-up of Fig. 5, since the leakage close-up is shown for negative pressure values. During the peak around 193 µs, a positive pressure build-up inside the chamber causes the second shutter to open even more, while negative pressure counteracts the leakage and reduces it. Hence, Fig. 5 already demonstrates the effects of asymmetry caused by the suspended shutter. Nevertheless, the overall effect is still relatively small, since besides the structural damping, the shutter movement is additionally damped by the squeeze film beneath the shutter [23]. To show the effect of Maxwell slip boundary conditions on the displacement, the shutter displacement in y-direction is depicted in Fig. 6. It is evident that the no-slip BC leads to higher overall displacement. The reason for this is that the no-slip BC restricts the air flow more, leading to a higher pressure build-up and, therefore, a higher force displacing the shutter. Finally, the effect of the suspension is compared by evaluating the negative pressure peak at a similar position to S1 but in the side channel. The results are shown in Fig. 7, where the time signal for the negative peak is shifted by half a period and multiplied by minus one to make the comparison easier. Again, two close-ups highlight the regions of interest. As it can be seen, the positive peak gets reduced slightly more when it comes to the overall peak of the pressure pulse. Nevertheless, the leakage seen in the time signal is less than for the

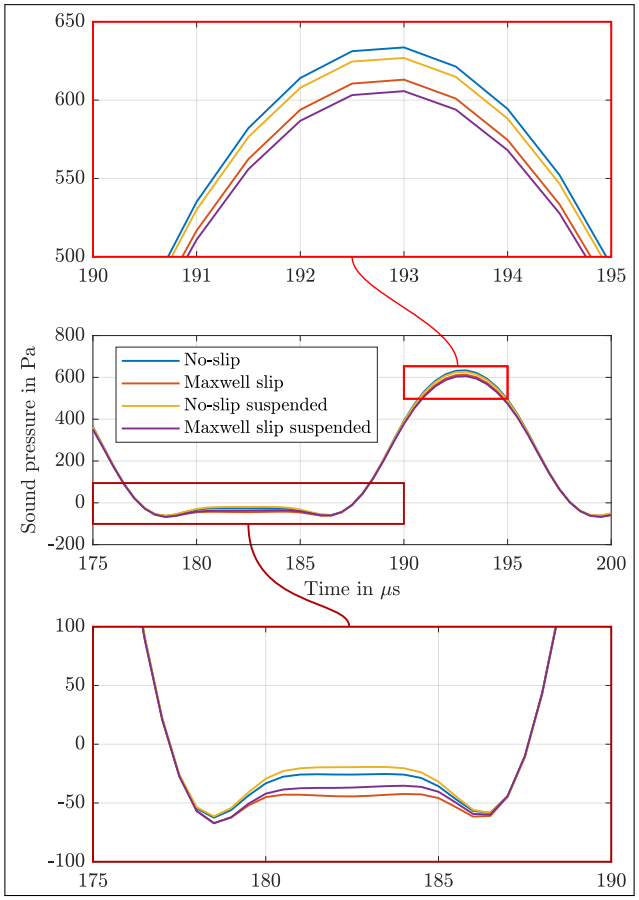

Figure 5. Sound pressure at S1 for four different setups.

negative sound pressure peak, which is the expected result from the introduced asymmetry. Overall, it can be said that the results clearly show the influence of non-linear effects, but the effect on the pressure peak is relatively small. The impact on the leakage shows a higher relative discrepancy, but the absolute deviation is still relatively small compared to the pressure peak. Nevertheless, the actual influence on parameters like total harmonic distortion needs to be investigated.

5. OUTLOOK

In this contribution, we have presented a highly coupled simulation workflow for ultrasound pulse-based sound generation principles, which can be used to investigate non-linear effects on the sound generation process. The

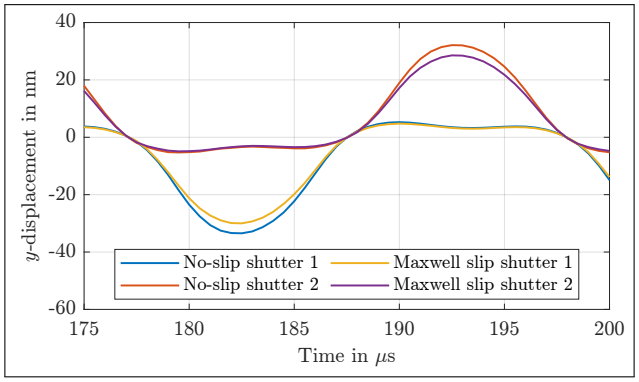

Figure 6. Comparison of the vertical shutter displacement for both shutters using either no-slip or Maxwell slip boundary conditions.

focus was laid on two effects for the presented investigation of resonant Advanced Digital Sound Reconstruction. On one hand, slip boundary conditions extended the validity of the underlying set of equations, which were used to incorporate effects in the slip flow regime. On the other hand, finite mounting stiffness was introduced, allowing the primarily horizontally moving shutter responsible for the modulation of the carrier signal to move normal to the prescribed movement direction. We have studied the various combinations of setups and their corresponding effects on the sound generation process. The introduction of slip boundary conditions has led to higher leakage, slightly reducing the overall usable sound pressure peak. Enabling the shutter to freely move in the vertical direction by incorporating realistic mounting stiffness introduced some asymmetry with respect to the achievable sound pressure pulse. The reason for the asymmetry is given by the movement of the shutter, which either constricts or expands the gap responsible for leakage, depending on the sign of the pressure pulse. Hence, it is advisable to ensure a stiff mounting situation in order to reduce asymmetry and adverse effects on the total harmonic distortion.

6. REFERENCES

[1] D. Tumpold, M. Stark, N. Euler-Rolle, M. Kaltenbacher, and S. Jakubek, "Linearizing an electrostatically driven MEMS speaker by applying pre-distortion," *Sensors and Actuators A: Physical*, vol. 236, pp. 289–298, 2015.

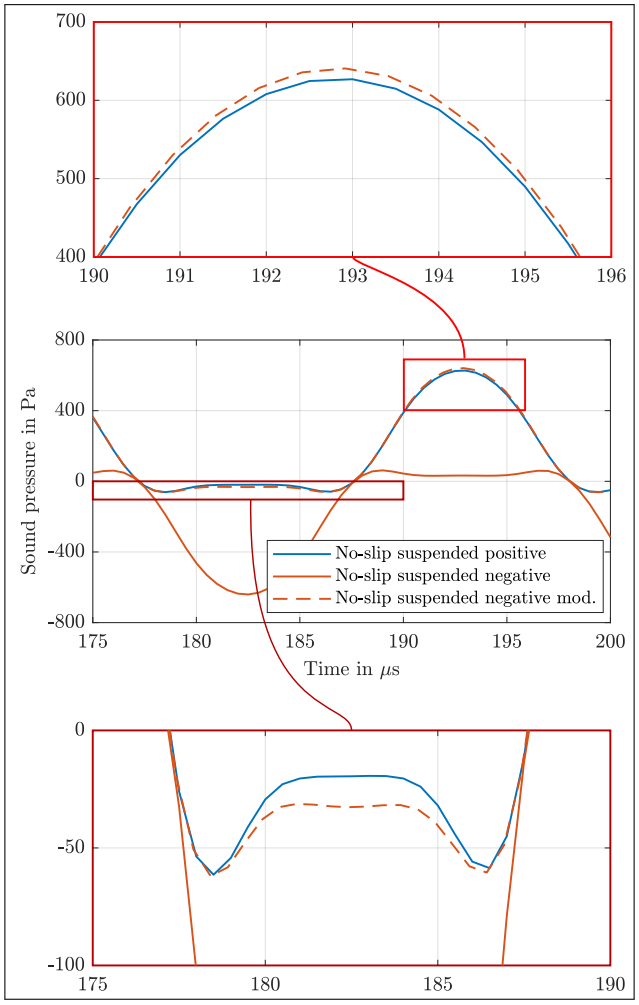

Figure 7. Comparison of the achievable sound pressure for no-slip boundary conditions using a suspended membrane. The dashed orange line represents a shifted and inverted version of the orange line for easier comparison.

[2] F. Stoppel, A. Männchen, F. Niekiel, D. Beer, T. Giese, and B. Wagner, "New integrated full-range mems speaker for in-ear applications," in *2018 IEEE Micro Electro Mechanical Systems (MEMS)*, pp. 1068–1071, 2018.

[3] R. Liechti, S. Durand, T. Hilt, F. Casset, C. Dieppedale, and M. Colin, "High performance piezoelectric mems loudspeaker based on an innovative wafer bonding process," *Sensors and Actuators*

A: Physical, vol. 358, p. 114413, 2023.

[4] M. Garud and R. Pratap, "Mems audio speakers*," *Journal of Micromechanics and Microengineering*, vol. 34, p. 013001, 11 2023.

[5] D. Mayrhofer, *A MEMS loudspeaker based on Advanced Digital Sound Reconstruction*. PhD thesis, TU Graz, 02 2024.

[6] S. Chen and M. Margalit, "Modulated ultrasound speakers - A common framework for analyzing air pump speakers," *Sensors and Actuators A Physical*, vol. 381, 2024.

[7] B. M. Diamond, J. J. Neumann, and K. J. Gabriel, "Digital sound reconstruction using arrays of CMOS-MEMS microspeakers," in *Technical Digest. MEMS 2002 IEEE International Conference. 15th IEEE International Conference on Micro Electro Mechanical Systems*, (Las Vegas, NV, USA), pp. 292–295, 2002.

[8] A. A. Arevalo Carreno, D. Conchouso Gonzalez, D. Castro, N. Jaber, M. Younis, and I. G. Foulds, "Towards a digital sound reconstruction MEMS device: Characterization of a single pzt based piezoelectric actuator," in *2015 IEEE 10th International Conference on Nano/Micro Engineered and Molecular Systems*, (Xi'an, China), pp. 290–295, 2015.

[9] D. Mayrhofer and M. Kaltenbacher, "Modeling and numerical simulations of mems shutter devices," in *WCCM-APCOM Congress 2022* (S. Koshizuka, ed.), Scipedia S.L., 2022.

[10] D. Mayrhofer, K. Roppert, D. Tumpold, and M. Kaltenbacher, "A moving mesh method for fluid-solid-acoustic interactions in mems devices," *Journal of Theoretical and Computational Acoustics*, vol. 32, no. 04, p. 2450016, 2024.

[11] H. Hassanpour Guilvaiee, *Modeling viscous and thermal effects in Micro-Electro-Mechanical System (MEMS) structures using the finite element method*. PhD thesis, TU Wien, Vienna, Austria, 2023.

[12] S. Roy, R. Raju, H. F. Chuang, B. A. Cruden, and M. Meyyappan, "Modeling gas flow through microchannels and nanopores," *Journal of Applied Physics*, vol. 93, no. 8, pp. 4870–4879, 2003.

[13] N. G. Hadjiconstantinou, "The limits of navier-stokes theory and kinetic extensions for describing small-scale gaseous hydrodynamics," *Physics of Fluids*, vol. 18, no. 11, p. 111301, 2006.

[14] N. Dongari, A. Sharma, and F. Durst, "Pressure-driven diffusive gas flows in micro-channels: from the knudsen to the continuum regimes," *Microfluidics and Nanofluidics*, vol. 6, pp. 679–692, 05 2009.

[15] G. Karniadakis, A. Beskok, and N. Aluru, *Microflows and Nanoflows Fundamentals and Simulation*, pp. 1–61. Interdisciplinary Applied Mathematics, Springer, 2005.

[16] A. Bhagat, H. Gijare, and N. Dongari, "Modeling of knudsen layer effects in the micro-scale backward-facing step in the slip flow regime," *Micromachines*, vol. 10, no. 2, 2019.

[17] M. Kaltenbacher, "openCFS." `https://www.opencfs.org`, 2025.

[18] K. Stein, T. Tezduyar, and R. Benney, "Mesh moving techniques for fluid-structure interactions with large displacements," *Journal of Applied Mechanics*, vol. 70, pp. 58–63, 01 2003.

[19] G. Link, M. Kaltenbacher, M. Breuer, and M. Döllinger, "A 2d finite-element scheme for fluid–solid–acoustic interactions and its application to human phonation," *Computer Methods in Applied Mechanics and Engineering*, vol. 198, no. 41, pp. 3321–3334, 2009.

[20] M. Kaltenbacher, *Numerical Simulation of Mechatronic Sensors and Actuators: Finite Elements for Computational Multiphysics*. Springer, 3 ed., 2015.

[21] D. Mayrhofer, T. Wilczacki, and M. Kaltenbacher, "Simulation of mems speakers using the linearized flow equations with maxwell slip boundary conditions," in *Proceedings of the 50th German Annual Conference on Acoustics (DAGA)*, (Stuttgart, Germany), pp. 1077–1080, 2024.

[22] D. Mayrhofer and M. Kaltenbacher, "Optimization of damping properties of acoustic mems shutter devices," in *Proceedings of the 10th Convention of the European Acoustics Association (Forum Acusticum 2023)*, (Torino, Italy), 2023.

[23] M. Bao, H. Yang, Y. Sun, and Y. Wang, "Squeeze-film air damping of thick hole-plate," *Sensors and Actuators A: Physical*, vol. 108, pp. 212–217, 11 2003.